VOL. 6, NO. 10, OCTOBER 2011 ISSN 1819-6608
ARPN Journal of Engineering and Applied Sciences


www.arpnjournals.com

THE CHARACTERISTICS OF THE VELOCITY FIELD IN A SLOT-VENTILATED WALL CAVITY

Akin Odewole and Rodger Edwards
School of Mechanical, Aerospace and Civil Engineering, The University of Manchester, Manchester, United Kingdom
E-Mail: cardilac2005@yahoo.com

ABSTRACT

Numerical investigations, using Reynolds Averaged Navier-Stokes (RANS) based methodology, were carried out to determine the characteristics of the velocity field in a thin wall cavity using rectangular slots with free ventilation area of about 3100 mm^2. The computation of the cavity flow in this study was based on three different flow modes: the pressure-driven, the buoyancy-driven and the combined pressure- and buoyancy-driven flow modes in a single-sided ventilation approach. The numerical results obtained with the computational fluid dynamics fluent package using the standard k-ε turbulence model show that a maximum velocity of about 6 m/s was obtained for ambient temperature ranging from -20 to 20^{o}C under the buoyancy-driven flow mode. This velocity of the cavity flow under this flow mode was shown to be significantly greater than a maximum velocity of about 1.5 m/s obtained under the pressure-driven and the combined flow modes. The predicted velocity fields for all flow modes employed in this study are characterized by multi-cellular patterns of airflow.

Keywords: cavity wall, ventilation slots, velocity field, buoyancy, turbulence, atmospheric boundary layer.

1. INTRODUCTION

The employment of cavity walls in the design and construction of building envelope has been shown to control the ingress of rainwater into buildings and thereby improve the moisture transport of the wall assembly (Oliver, 1988; Stovall and Karagiozis, 2004). By ventilating the cavity in these walls, a reduction in the thermal load of the buildings will result in an improvement in the comfort of the occupants while condensation of moisture-laden air in the winter may also be prevented. Recently, it has become a mantra among architects and other building professionals to ventilate cavity walls by locating holes of any size and shape on the building façade based on the expectation that a little air movement will keep the cavity dry.

Although natural ventilation of the wall cavity is governed by a number of factors, including: solar radiation; size and position of ventilation openings; turbulence; wind speed and direction (Etheridge and Sandberg, 1996; Li and Delsante, 2001), knowledge of the ventilation process within this cavity is however limited at present. The aim of the present study is therefore to numerically investigate the characteristics of the velocity field in a slot-ventilated wall cavity under the pressure- and buoyancy-driven flow modes and the combined pressure- and buoyancy-driven flow mode. The paper starts with a description of the problem in section 1 while the numerical techniques employed for the study are described in section 2. In section 3, the results of the investigations are presented and discussed while suitable conclusions are drawn from the study in section 4.

2. METHODOLOGY

2.1 Computational model and analysis

The system under investigation is an empty three-dimensional cavity shown in Figure-1. The interior of the cavity constitutes the flow domain and is filled with air. The cavity has flow inlets and outlets (ventilation slots) located on the same side of its outer wall, forming a single-sided ventilated cavity. In order to prevent rainwater ingression into the cavity, the lower ventilation slots are located at 100mm above the ground level. This spacing of the lower ventilation slots from the ground level is maintained for all sides of the cavity's front wall. As a result of this spacing, the upper ventilation slots assume a near ceiling-slot inlet arrangement. The wind flow over the building façade enclosing the cavity is a wind-driven pressure regime and in a perpendicular direction to the façade. The lower ventilation slots in Figure-1 fall into the inner region of the atmospheric boundary layer, which exists just above the ground. In this region, the wind is affected by frictional forces exerted by structures such as trees, buildings and fences on the surface of the earth. This causes the intensity of turbulence due to the wind arising from such structures on the earth surface to be high at locations very close to the ground.

The magnitude of the turbulent intensity in this region depends on the nature of the terrain at or around the site of buildings (Levermore, 2000). However at higher locations above the ground level, the intensity of the turbulence decreases with height. Thus, the average wind speed increases with height above the ground. This causes a variation in the profiles of mean wind speed from different terrains (Mendis *et al*., 2007). Since lower wind speeds are obtained very close to the ground in comparison with higher locations above the ground, lower wind pressures are therefore obtained at regions very close to the ground (Equation-1) in contrast to higher wind pressures at higher locations above the ground,

$$p_w = 1/2\, c_p \rho_o w_h^{\,2}. \qquad \ldots\ldots (1)$$

where

p_w = mean pressure due to the wind flow on to or away from a surface,

c_p = static pressure coefficient,

ρ_o = reference air density, and

w_h = reference wind speed at a datum level (usually at the height of a building or opening).

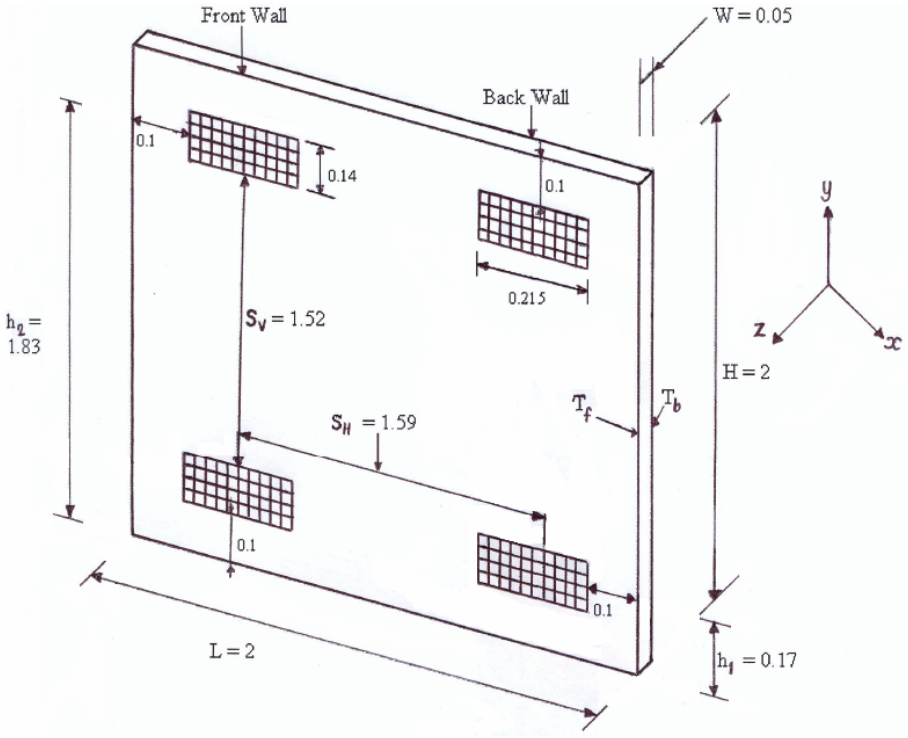

Figure-1. Configurations and dimensions (not drawn to scale) of the wall cavity, showing the ventilation slots. Square grids on the slots represent the ventilation baffles on these slots. All dimensions are in metres.

The reference wind speeds w_{h_1} and w_{h_2} at the position of the lower and upper ventilation slots are obtained by correcting the meteorological wind speed, v_m (Table-1) from a weather station to the wind speeds on the site of a building (Equation-2). In Equation (2); v_m is the mean wind speed at 10 m height in open country, K_s (= 0.35) is a parameter relating the wind speed to an urban terrain, and a (= 0.25) is an exponent relating the wind speed to the height above the ground (Levermore, 2000). Airflow, driven by the wind pressure difference, Δp_w defined in Equation (3) between the lower and upper ventilation slots separated by a vertical distance, S_v enters the wall cavity through the inlets (upper ventilation slots). The arrangement of the inlet slots near the cavity's front wall is known as a lateral inlet slot design and has been shown to improve the homogeneity of airflow distribution and the ventilation efficiency of an enclosure in contrast to centrally located inlet slots (Moureh and Flick, 2005; Moureh *et al*., 2009). The insect baffles on the ventilation slots in Figure-1 offer a large resistance to the airflow and therefore produce a free ventilation area of about 3100 mm^2. A square cross-section, with height H and width L, respectively for the front and back wall of the cavity is employed for this study. Air layers, with a thickness W are thus enclosed between the walls of the cavity. The height and width of the cavity in this study are therefore chosen to correspond to the minimum floor-to-ceiling distance in most low-rise residential buildings (Barry, 1996; Waters, 2007; Building Regulations A, 2000).

$$w_h = v_m K_s h^a. \quad \text{..... (2)}$$

$$\Delta p_w = p_{w_{h2}} - p_{w_{h1}} = 1/2 c_p \rho_o \left({w_{h_2}}^2 - {w_{h_1}}^2 \right) = 1/2 c_p \rho_o \Delta {w_h}^2. \quad \text{..... (3)}$$

Table-1. Reference wind speed, w_h (m/s) and pressure difference, Δp_w (Pa) for the wall cavity ventilation. The height, H of the cavity is 2m.

v_m*	w_{h_1}	p_{w_1}	w_{h_2}	p_{w_2}	Δp_w
2.4	0.5	0.11	1.0	0.45	0.34
4.8	1.1	0.55	2.0	1.81	1.26

*: v_m are obtained from the Manchester (Ringway) meteorological station using CIBSE Guide J, 2002.

Three ambient temperatures; -20°C (253.15K), 1°C (274.15K) and 20°C (293.15K) are employed in the computation of the cavity flows under the buoyancy-driven flow mode. Temperatures of -20°C (253.15K) and 20°C (293.15K) represent extreme conditions of winter and summer temperatures respectively while 1°C (274.15K) is a borderline condition between the two extreme temperature conditions. The choice of these ambient temperatures against a fairly constant back wall temperature, T_b of 283.15K (assuming the interiors of buildings are well insulated) will enable the velocity characteristics of the wall cavity to be compared under certain stack (or buoyancy) and wind pressure differences. Thus, airflow into the wall cavity in Figure-1 also occurs by virtue of the stack (or buoyancy) pressure difference, Δp_s between the ambient air and that within the cavity. The stack pressure difference between two openings separated by a vertical distance, S_v is given as shown in Equation (4) (Awbi, 2003) where g is the gravitational acceleration, T_o is the ambient air temperature and T_i is the inner cavity temperature. An estimate of the inner cavity temperature T_i is given in Equation (5) while distances S_H (the horizontal separation between the ventilation slots) and S_v are based on measurements from the centroid of all ventilation slots.

$$\Delta p_s = -\rho_o g S_v (1 - T_o / T_i). \quad \ldots\ldots (4)$$

$$T_i \equiv T_m = \frac{T_f + T_b}{2}. \quad \ldots\ldots (5)$$

For the computation of the buoyancy-driven flows therefore, the front and back walls of the cavity are modelled as isothermal but differentially heated surfaces. Under this condition, the front wall of the cavity is prescribed with a uniform temperature T_f while the back wall of the cavity is prescribed with a uniform temperature T_b. However, the connecting walls are made perfectly insulated (adiabatic). The temperature of the cavity's front wall, T_f is assumed to be the same as that of the ambient, T_o. The numerical modelling approach employed in this study offers the unique advantage of separate and combined evaluation of the pressure and buoyancy forces influencing airflow in the wall cavity studied. It is difficult to separate pressure and buoyancy forces during measurement in a real building. The use of CFD to numerically predict the characteristics of airflow in a slot-ventilated wall cavity therefore helps in a better understanding of the separate and combined effects of pressure and buoyancy (or stack) forces in the wall cavity.

In the third modelling approach, the buoyancy-driven approach of flow computation is combined with the pressure-driven mode. Six different flow cases are considered here. For these cases, wind pressure differences of 0.34 and 1.26Pa are compared against stack pressure differences of 0.34, -0.34 and -1.27Pa (Table-2). These cases, arising from the selective combination of these stack and wind pressure differences together, will help in establishing whether reinforcing or counteracting flows are obtainable under the different modelling conditions employed in this study. The properties of the air layers in the wall cavity in all the modelling approaches are evaluated at a mean temperature, T_m. The stack (or buoyancy) pressure differences of -0.34 and 0.34Pa in Table-2 are similar to a wind pressure difference, Δp_w of 0.34Pa in Table-1 while the stack pressure difference, Δp_s of -1.27Pa in Table-2 is comparable to a wind pressure difference, Δp_w of 1.26Pa in Table-1.

Table-2. Stack pressure differences for a range of ambient temperature.

Ambient temperature	**Inner cavity temperature**	**Density** ρ_o	**Stack** (Buoyancy) **pressure difference**
T_o (K)	T_i (K)	(kg/m^3)	Δp_s (Pa)
253.15	268.15	1.389	-1.27
274.15	278.65	1.289	-0.34
293.15	288.15	1.205	0.34

2.2 Boundary conditions

In this study, adiabatic walls are used except for the two isothermal walls employed in the computation of the buoyancy-driven flows. The isothermal walls consist of the front or outer wall and the back or inner wall and are differentially heated. The front wall is prescribed with

a uniform temperature, T_f while the back wall is prescribed with a uniform temperature, T_b. Thus, the boundary conditions for the wall cavity modelled in this study can be written as:

$$T = T_b \text{ at } z = 0 \quad (6)$$

$$T = T_f \text{ at } z = W \quad (7)$$

$$\frac{\partial T}{\partial y} = 0 \text{ at } y = 0 \text{ and } y = H \quad (8)$$

$$\frac{\partial T}{\partial x} = 0 \text{ at } x = 0 \text{ and } x = L \quad (9)$$

The no-slip velocity boundary conditions are prescribed on all cavity walls and shown in Equation (10).

$$u = v = w = 0 \text{ at } x = 0,\ x = L,\ y = 0 \quad (10)$$
$$y = H,\ z = 0,\ z = W$$

The computational domain, consisting of bounding solid walls, whose boundary conditions are as given in Equations (6) to (10) above, is also surrounded by flow inlets and outlets. Uniform distribution is assumed for the kinetic energy of turbulence k, turbulent energy dissipation rate ε and the velocity component, w_{h_2} at the flow inlets. At the inlet boundaries therefore, $u_{h_2} = v_{h_2} = 0$ while w_{h_2} takes two values: 1 and 2m/s. These velocity values are typical incident wind speeds for ventilation application (Edwards, 2005). The turbulent kinetic energy, k at the flow inlets is expressed as shown in Equation (11) where I, expressed as per cent, represents the turbulence intensity of the z-velocity component at the inlets while the turbulent dissipation rate, ε is expressed as shown in Equation (12) (Versteeg and Malalasekera, 1995). D_H represents the hydraulic diameter of the inlet section and is used for calculating the inlet-based Reynolds number for determining if a flow is laminar or turbulent. C_μ is an empirical constant, with a value of 0.09 (Launder and Spalding, 1972). Uniform distribution was assumed for k and ε at the inlets while uniform pressure assumption and zero gradients for all transport variables were applied at the outflows.

$$k = 3/2\left(w_{h_2} I\right)^2. \quad (11)$$

$$\varepsilon = \frac{C_\mu^{0.75} k^{1.5}}{0.07 D_H}. \quad (12)$$

2.3 Turbulence model

For modelling turbulence in the cavity flow, the standard $k-\varepsilon$ turbulence model, using wall functions of the non-equilibrium type, for bridging the viscosity-affected near-wall regions with the fully turbulent core was employed (Fluent, 2006). The choice of this model was based on its performance in producing fairly accurate results in comparison with those of the RNG and Realizable models under similar modelling conditions (Odewole and Edwards, 2010). The equations governing the incompressible, steady turbulent cavity flow in this study are the Reynolds-averaged Navier-Stokes (RANS) equations shown in conservative forms in Equations (13) and (14) below. Equation (13) is for the conservation of mass while Equation (14) is for the conservation of momentum. The energy term shown in Equation (15) is used since the Boussinesq approximation is employed in formulating the fluid density, ρ. For further information on the $k-\varepsilon$ turbulence model and its application, the following literatures may be found useful: Launder and Spalding, 1972; Daly and Harlow, 1970; Versteeg and Malalasekera, 1995 and Patankar, 1980.

$$\rho \frac{\partial}{\partial x_i}\left(u_i\right) = 0. \quad (13)$$

$$\frac{\partial}{\partial x_j}\left(\rho u_i u_j\right) = -\frac{\partial p}{\partial x_i} + \frac{\partial}{\partial x_j}\left[\mu\left(\frac{\partial u_i}{\partial x_j} + \frac{\partial u_j}{\partial x_i} - \frac{2}{3}\delta_{ij}\frac{\partial u_l}{\partial x_l}\right)\right] + \frac{\partial}{\partial x_j}\left(-\overline{\rho u_i' u_j'}\right) + g\beta\rho\Delta T. \quad \text{…….. (14)}$$

$$\frac{\partial}{\partial x_j}(\rho u_j T) = \frac{\partial}{\partial x_j}\left(\frac{\mu}{\Pr}\frac{\partial T}{\partial x_j} - \overline{\rho u_j t}\right). \quad \text{…… (15)}$$

2.4 Numerical scheme and method of solution

Meshes of high density, using non-uniform grid size, were employed for discretizing the computational domain into numerous control volumes, with the size of the smallest control volumes close to the walls being 0.008m. A grid independence study undertaken gives a performance advantage of 27% (difference in the value of the skin friction coefficient, c_f between the two finest meshes employed in the numerical study) do marginally justify a 20% increase in the cell number obtained in the mesh refinement between the two finest meshes. The optimum mesh density employed in this numerical study

therefore enables sufficient details of the velocity fields to be obtained. By employing FLUENT, a commercial Computational Fluid Dynamics (CFD) code using the finite volume approach, the equations governing the cavity flow were solved sequentially in a segregated manner using a pressure-based solver with the Gauss-Siedel iterative procedure.

The convection terms were obtained using the second order upwind scheme while the second-order accurate central-differencing scheme was employed for the diffusion terms of the governing equations. The PRESTO! Scheme, applicable to all meshes and suitable for computing the face pressure using the discrete continuity balance for a "staggered" control volume similar to that of Patankar (1980) was employed for the pressure interpolation in Equation (14) while interactions between pressure and velocity in Equations (13) and (14) were coupled using the SIMPLE algorithm (Moureh and Flick, 2005; Fluent, 2006). Convergence of the incompressible, steady turbulent cavity flow was checked by ensuring that scaled residuals were less than 10^{-4} for all variables, except the energy term where the scaled residual was less than 10^{-6}. To ensure the stability of the numerical simulations, under-relaxation was applied in the numerical scheme.

3. RESULTS AND DISCUSSIONS

The pressure-driven velocity fields shown in Figure-2 are characterized by two recirculation regions of different size.

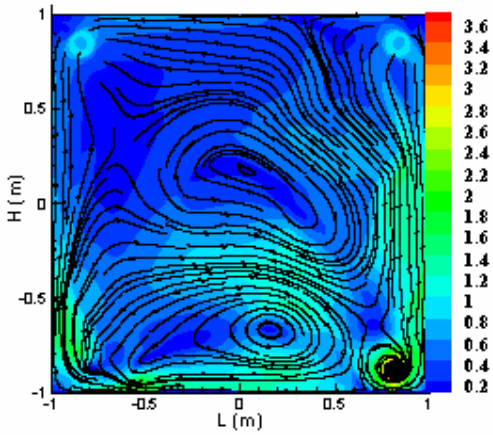

(a)

The existence of these multiple recirculation regions, also called multi-cellular or secondary flows (Lartigue *et al*., 2000; Elder, 1965) is attributed to the small free ventilation area of about 3100 mm^2 provided by the slots and causes the flow of airstream into the wall cavity to be in the form of high speed air jets, with high momentum and energy transfer associated with the flow. With an increase in the wind pressure difference, Δp_w driving the flow from 0.34 to 1.26 Pa, the average velocity of the cavity flow increases. Higher velocities are also experienced in the vertical near-wall regions in contrast to other areas of the cavity. A characteristic feature of the cavity flows shown in Figure-2 is the existence of multiple recirculation cells with irregular shape and size caused by fluctuation or unsteadiness associated with the flow of the wind.

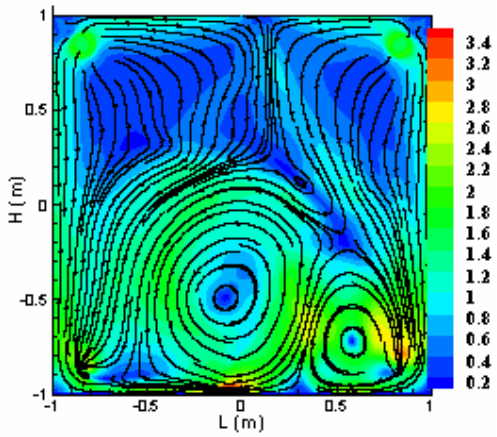

(b)

Figure-2. Pressure-driven velocity fields (m/s) from the slot-ventilated cavity: (a) $\Delta p_w = 0.34Pa$ (b) $\Delta p_w = 1.26Pa$.

The unsteadiness in the airstream entering the inlet slots into the wall cavity is therefore responsible for the unsymmetrical nature of the multi-cellular flow patterns obtained under the pressure-driven flow mode present in Figure-2 and the low velocities associated with these flows. The unsteadiness in the cavity flows driven by the wind pressure difference, Δp_w is also evident in the irregular x-velocity distributions shown in Figure-3 where the average velocities of the cavity flows increase as the wind pressure difference, Δp_w increases.

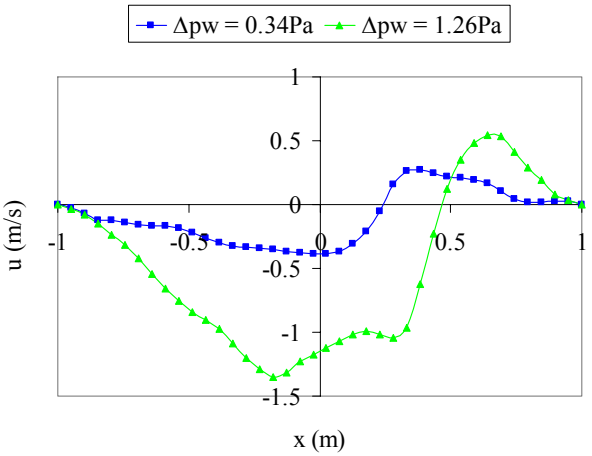

Figure-3. Pressure-driven x-velocity distributions (m/s) from the slot-ventilated cavity.

In Figure-4 where the buoyancy (stack) pressure difference, Δp_s drives the cavity flow; regular and symmetrical patterns of airflows are obtained. Here, two large recirculation cells of similar shape and size are obtained in the wall cavity for varying stack pressure difference, Δp_s . The average velocities of the cavity flows in Figure-4 are therefore significantly higher than that of Figure-2 under similar or comparable wind pressure differences. The symmetrical nature of the cavity flows under the buoyancy-driven flow mode is also evident in Figure-5 where comparable distributions of the x-velocity of the cavity flows, with a maximum velocity of about 6m/s, are obtained. These comparable velocity distributions are in agreement with the similar or comparable velocity fields present in Figure-4.

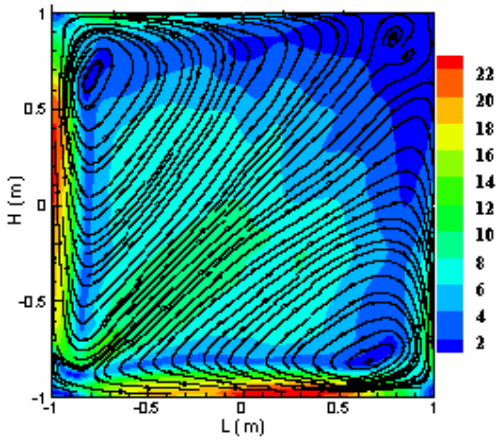

(a)

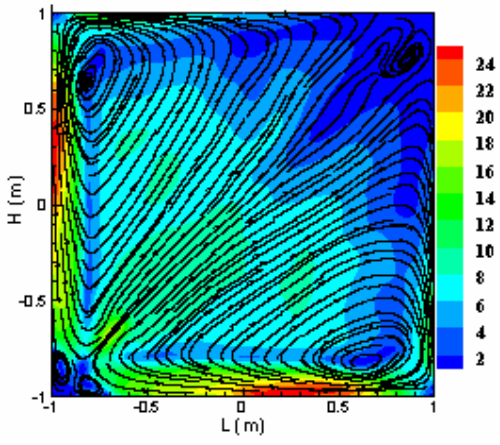

(b)

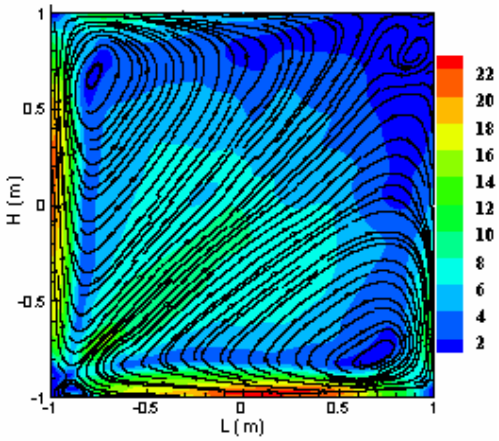

(c)

Figure-4. Buoyancy-driven velocity fields (m/s) from the slot-ventilated cavity: (a) $\Delta p_s = -1.27Pa$ (b) $\Delta p_s = -0.34Pa$ (c) $\Delta p_s = 0.34Pa$

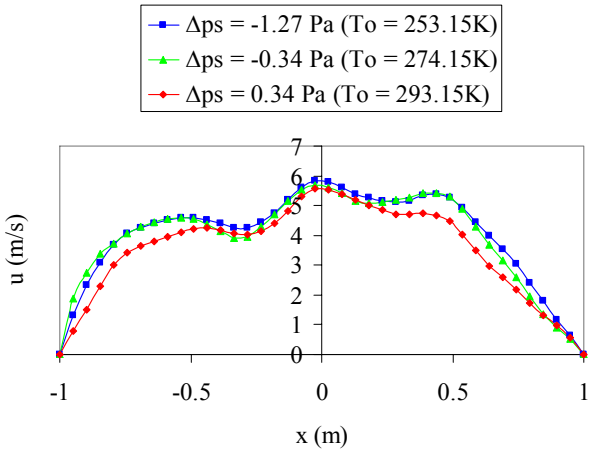

Figure-5. Buoyancy-driven x-velocity distributions (m/s) from the slot-ventilated cavity.

The regular size of the multi-cellular cells and the symmetrical nature of the cavity flows in Figure-4 under the buoyancy-driven flow mode are destroyed in Figures 6 and 8 where stack pressure differences of 0.34 and 1.27Pa are combined with wind pressure differences of 0.34 and 1.26 Pa under different modelling conditions. In Figure-6, similar or comparable wind and stack pressure differences are combined together. The inner cavity temperature, T_i in Figures 6(a) and 6(b) is greater than the ambient temperature, T_o in these two cases. As a result, the less dense air in the wall cavity flows in a vertical upward direction. The rising airstream, which is driven by the stack pressure difference, Δp_s exits the wall cavity through the upper ventilation slots. The passage of the hot airstream in these two cases therefore coincides with the entry of colder airstream driven by the wind pressure

difference, Δp_w from the ambient. These opposing airflows, driven by similar or comparable wind and stack pressure differences in these instances, result in the destructive interference of the cavity flows. The average velocities of flows in Figures 6(a) and 6(b) are therefore lower than those in Figures 4(a) and 4(b) and of similar or comparable values to those of Figure-2.

In Figure-6(c) however, downward flow of air due to similar wind and stack pressure differences occurs in the same direction and through the upper ventilation slots. In this instance, a constructive interference from both flows is obtained. This causes the average velocity of the cavity flow in Figure-6(c) to be slightly higher than that of Figure-2. Although it might be expected that the average velocity of the cavity flow in Figure-6(c) will be higher than that of Figure-4(c) since a constructive flow is obtained in Figure-6(c) under this combined flow mode, the unsteadiness associated with the cavity flow in Figure-6(c) due to the combination of airflow from the wind and stack pressure differences through the inlet slots is responsible for its average velocity being lower than that of Figure-4(c).

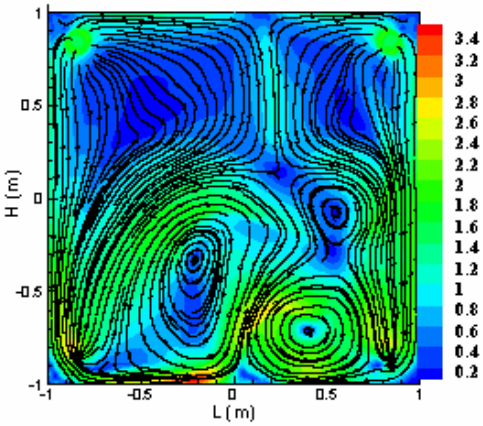

(a)

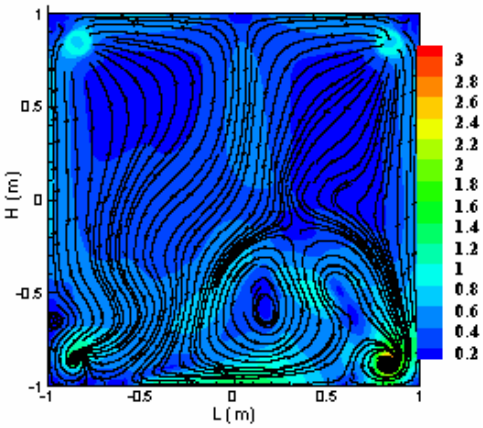

(b)

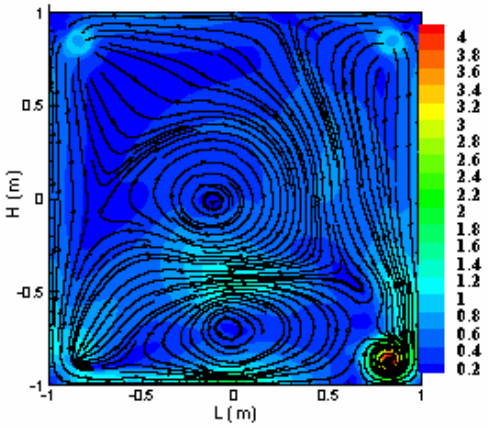

(c)

Figure-6. Combined flow mode velocity fields (m/s) from the slot-ventilated cavity for similar or comparable wind and stack pressure differences:

(a) $\Delta p_s = -1.27Pa$ and $\Delta p_w = 1.26Pa$

(b) $\Delta p_s = -0.34Pa$ and $\Delta p_w = 0.34Pa$

(c) $\Delta p_s = 0.34Pa$ and $\Delta p_w = 0.34Pa$

The reduction in the average velocities of the cavity flows when similar or comparable wind and stack pressure differences are combined together becomes more evident in Figure-7, where the average velocities of cavity flows are significantly lower than those driven only by the buoyancy forces in Figure-5.

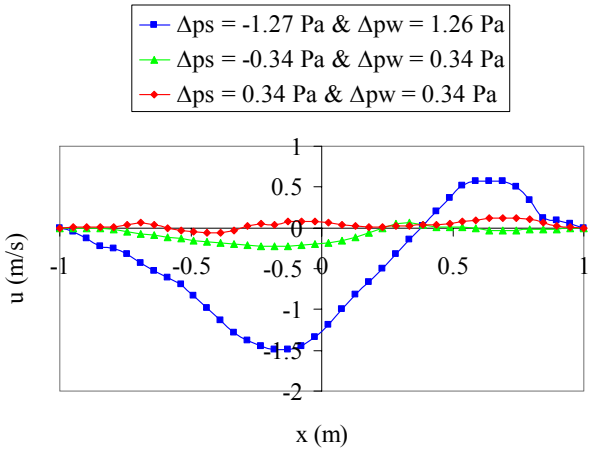

Figure-7. Combined flow mode x-velocity distributions (m/s) from the slot-ventilated cavity for similar or comparable wind and stack (buoyancy) pressure differences.

In Figure-8, different wind and stack pressure differences are combined together. Higher average velocity of cavity flow may also be expected in Figure-8(a) where the stack (buoyancy) pressure difference, Δp_s (1.27Pa) is significantly greater than the wind pressure

difference, Δp_w (0.34Pa) but the opposing nature of these two flows, combined with the fluctuating characteristics of the wind flow, is responsible for the low average velocity of flow obtained. In Figure-8(b) where the wind flow and the stack flow travel through the same upper ventilation slots into the wall cavity, the average velocity of the cavity flow is higher than that of Figure-6(c) under similar flow direction since Δp_w of 1.26Pa is significantly greater than Δp_s of 0.34Pa. In Figure-8(c), opposing flows similar to that of Figure-8(a) are obtained. Here, greater fluctuations are associated with the wind flow ($\Delta p_w = 1.26Pa >> \Delta p_w = 0.34Pa$). As a result, higher average velocity of flow is obtained in Figure-8(c) in contrast to Figure-8(a). This is evident in the combined x-velocity distributions shown in Figure-9 under different wind and stack (buoyancy) pressure differences.

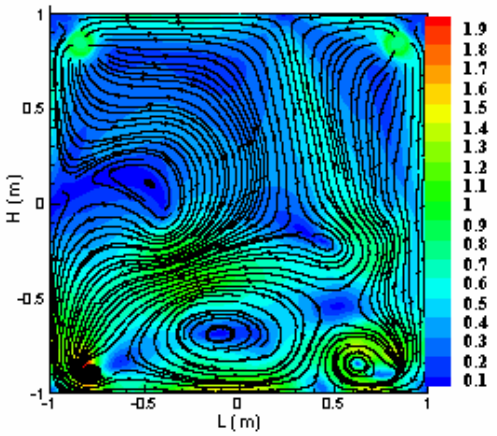

(a)

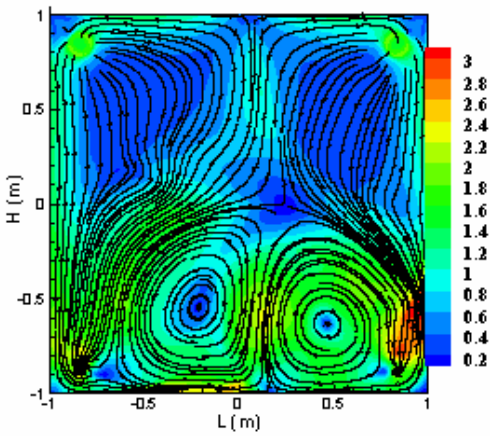

(b)

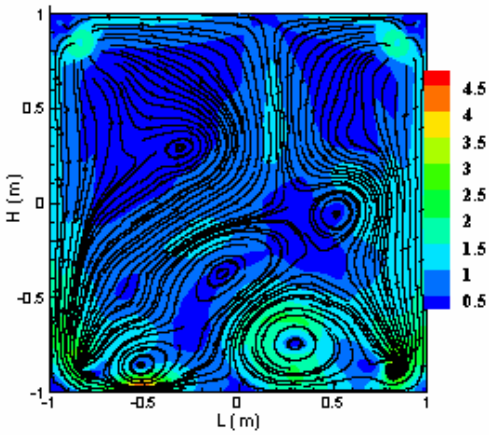

(c)

Figure-8. Combined flow mode velocity fields (m/s) from the slot-ventilated cavity for different wind and stack pressure differences: (a) $\Delta p_s = -1.27Pa$ and $\Delta p_w = 0.34Pa$ (b) $\Delta p_s = 0.34Pa$ and $\Delta p_w = 1.26Pa$ (c) $\Delta p_s = -0.34Pa$ and $\Delta p_w = 1.26Pa$

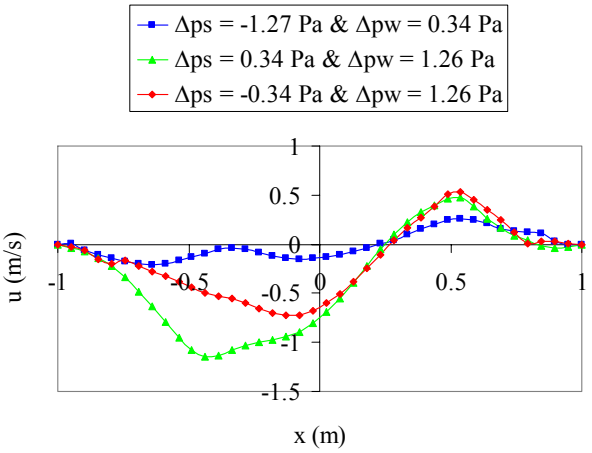

Figure-9. Combined flow mode x-velocity distributions (m/s) from the slot-ventilated cavity for different wind and stack (buoyancy) pressure differences.

4. CONCLUSIONS

Numerical flow modelling in a thin slot-ventilated wall cavity (W/H = 0.025) under three flow modes was carried out in this study using rectangular ventilation slots. The results of the investigations show multi-cellular airflow patterns for all the velocity fields in Figures 2, 4, 6 and 8 under different modelling and simulation conditions. The occurrence of the multi-cellular flow patterns offers great potential for the remediation of moisture in the slot-ventilated wall cavity studied. Interactions among the multiple recirculation cells cause the fluctuation or unsteadiness in the cavity flows to increase.

The increased fluctuation in the cavity flows generates other secondary motion that further mixes the fluid. These motions in the wall cavity cause a continuous disruption of the thin boundary layer in the vicinity of the cavity walls and therefore result in an increased turbulence of the cavity flows. The thickness of the viscous sub-layer is thus subsequently reduced while the average velocities of the cavity flows increase. The thermal barrier between the cavity fluid and the walls for the temperature-dependent flows (buoyancy-driven flows) is also lowered. This increases the Nusselt number of the cavity flows in contrast to unicellular flows (Garcia *et al*., 2005). Also, the turbulent nature of the multi-cellular flow patterns ensures that all corners of the cavity are reached. Unventilated pockets of air in these regions are therefore replaced by fresh air supply from the ambient.

For cavity flows under the combined flow mode, counteracting flows with reduced average velocities in contrast to the buoyancy-driven flows are obtained when similar or comparable wind and stack pressure differences are combined together irrespective of the direction of each flow. Similar counteracting effect is obtained if Δp_s is significantly greater than Δp_w for opposing flows. If Δp_w is however significantly greater than Δp_s, reinforcing flows are obtained irrespective of the direction of each flow. In all these instances of the combined flow mode, the average velocities of the cavity flows are lower than those for the buoyancy-driven flows.

ACKNOWLEDGEMENTS

The authors greatly acknowledge the financial assistance provided by both English Heritage and Irish Heritage in carrying out these investigations.

REFERENCES

Oliver A.C. 1988. Dampness in Buildings, BSP Professional Books, England.

Stovall TK, Karagiozis A. 2004. Airflow in the ventilation space behind a rain screen wall. In: Performance of Exterior Envelopes of Whole Buildings 9th International Conference, ASHRAE.

Etheridge D., Sandberg M. 1996. Building Ventilation: Theory and Measurement, John Wiley and Sons, England.

Li Y, Delsante A. 2001. Natural ventilation induced by combined wind and thermal forces. Building and Environment. 36: 59-71.

Waters JR. 2007. Ventilation. In: The Building Regulations, Blackwell Publishing, England.

Barry R. 1996. Walls In: The Construction of Buildings 1. Blackwell Science Ltd, England.

Fluent 6.3 User's Guide. 2006. Fluent Inc., 10 Cavendish Court, Lebanon, NH 03766, USA.

Odewole A and Edwards R. 2010. Simulation of airflow patterns within wall cavities. In: TG75 Engineering Studies on Traditional Constructions. Proceedings of the CIB World Congress, Salford, Manchester, UK. pp. 1-12.

Launder BE and Spalding DB. 1972. Mathematical Models of Turbulence, Academic Press Inc. England.

Daly BJ and Harlow FH. 1970. Transport equations in turbulence. Phys. Fluids. 13: 2634-2649.

Patankar SV. 1980. Numerical Heat Transfer and Fluid Flow. Hemisphere Publishing Corporation, N.Y., USA.

Levermore GJ. 2000. Building Energy Management Systems: Applications to Low-Energy HVAC and Natural Ventilation Control. E and FN Spon, London, UK.

Mendis P, Ngo T, Haritos N, Hira A, Samali B and Cheung J. 2007. Wind loading on tall buildings. EJSE International. 7: 41-54.

Moureh J and Flick D. 2005. Airflow characteristics within a slot-ventilated enclosure. Int. J. Heat and Fluid Flow. 26: 12-24.

Moureh J, Tapsoba M and Flick D. 2009. Airflow in a slot-ventilated enclosure partially filled with porous boxes: Part I - Measurements and simulations in the clear region. Computers and Fluids. 38: 194-205.

The Building Regulations. 2000. Approved Document A: Structure, National Building Specification, London.

Awbi HB. 2003. Ventilation of Buildings. Spon Press, London, UK.

CIBSE Guide J. 2002. Weather, Solar and Illuminance Data. The Chartered Institution of Building Service Engineers, London, UK.

Edwards R. 2005. Handbook of Domestic Ventilation. Elsevier Butterworth and Heinemann, England.

Versteeg HK and Malalasekera, W. 1995. An Introduction to Computation Fluid Dynamics: The Finite Volume Method. Pearson Education Ltd, England.

Lartigue B, Lorente S and Bourret B. 2000. Multi-cellular natural convection in a high aspect ratio cavity: Experimental and numerical results. Int. J. Heat Mass Transfer. 43: 3157-3170.

Elder JW. 1965. Laminar free convection in a vertical slot. J. Fluid Mechanics. 23: 77-98.

Garcia A, Vicente PG and Viedma A. 2005. Experimental study of heat transfer enhancement with wire coil inserts in laminar-transition-turbulent regimes at different Prandtl numbers. Int. J. Heat Mass Transfer. 48: 4640-4651.